# Miniature 3D Microscope and Reflectometer for Space Exploration

Gustav M. Pettersson[1,2], Michael Dille[3], Sara Abrahamsson[2], and Uland Wong[3]
[1]Aeronautical and Vehicle Engineering, KTH Royal Institute of Technology, Sweden
[2]Electrical and Computer Engineering, University of California Santa Cruz
[3]Intelligent Robotics Group, NASA Ames Research Center

**Characterization of objects in all dimensions at a microscopic level is important in numerous applications including surface analysis on planetary bodies. Existing microscopes fit for this task are large bench-top devices unsuitable for in-situ use, particularly in resource-constrained remote robotic exploration. Computational imaging techniques present a powerful means to overcome physical limitations in fielded sensors, but have seen especially little use in space applications. We present a miniature (150 gram) 3D microscopic imager without moving parts capable of providing 1-megapixel images at approximately 1 micron horizontal and 5 micron vertical resolution. This device combines light-field imaging and photometric stereo to provide both 3D reconstruction and reflectance characterization of individual soil grains. We thoroughly evaluate its performance by designing and nanofabricating a 3D-fiducial and further demonstrate its operation on a library of planetary soil simulants. This system opens vast opportunities for extension, demonstrating the potential of computational imaging to amplify sensing capabilities in space.**

***Index Terms*—3D-microscopy, multi-view stereo, gonioreflectometry, planetary exploration, computational photography**

## I. Introduction

MICROSCOPIC characterization is an invaluable tool across applications including the study of surface materials on planetary bodies, analysis of rocks on earth, hazardous material identification, and defect testing during manufacturing or construction. Microscopy has therefore become a ubiquitous method to inspect samples and collect detailed data. Carrying versatile microscopic imagers in space is common, with the Mars Hand Lens Imager (MAHLI) [1] aboard the Curiosity rover the most prominent example. However, MAHLI does not have sufficient resolution to inspect and map the grains of regolith (soil), with tasks such as measuring grain size and composition conducted by other science payloads. Future exploration studies are focused on small and versatile robotic platforms which can reach currently inaccessible environments and cover large areas, for which the resources available for science payloads are highly restricted. We therefore propose an in-situ miniature 3D microscope delivering grain-of-sand resolution micrographs combined with powerful computational imaging methods such as 3D modeling and reflectometry. With this device, samples can be remotely studied in depth and with versatility akin to having a sample in the lab.

Many data gathering tasks occur in harsh or remote locations that complicate both the collection of samples to return to a lab for study or the use of large, fragile imaging equipment. These constraints are found in terrestrial remote sensing and field exploration scenarios, but the motivating application for this work is planetary exploration, which by necessity is remotely conducted. Areas inaccessible to existing rovers are gathering increasing interest, including steep hills, ravines, or rubble-filled caves. A variety of possible systems to reach these have been proposed, among them hoppers [2], climbers [3], and rotorcraft [4]. Typically deployed as small daughtercraft, these commonly share the constraints of low size, mass, and power, as well the need to withstand the

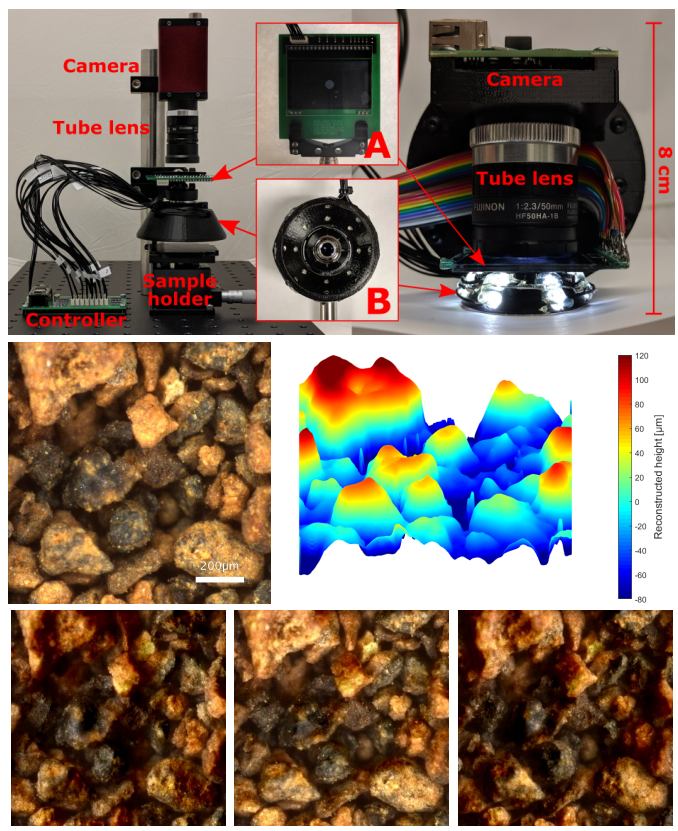


Fig. 1. Top: Montage of the two prototype microscopes built for this work. Inset A: A transparent LCD is used to control the aperture and therefore the viewing direction without physical motion. Inset B: A constellation of LEDs surrounding the objective lens is used to control the illumination direction. Middle: Image of *JSC Mars-1* simulant and reconstructed height from fused MVS and PS data. Bottom: Synthetically lit scenes from PS data with a single light source placed at (L to R): 30° elevation from the left; 60° elevation from beneath; 30° elevation from the right. These rendered views do not correspond to the captured data which are illuminated from 22.5° and 45°.

Corresponding author: G. M. Pettersson (Email: gupet@kth.se)

shock of landing or emplacement. Interest in this paradigm has resulted in many designs of robotic explorers, but little work has been done to adapt scientific instrumentation. To fill this role, compact, efficiently battery powered, solid-state payloads must be developed which can provide the deep scientific insights desired from these environments.

Our 3D microscopic imager consists of a single optical pathway and has no moving parts. Instead, it incorporates two complementary mechanisms for deriving 3D information: A transparent liquid crystal display (LCD) in the optical pathway enables a programmable aperture and thereby viewpoint, while a hemispherical constellation of light emitting diodes (LEDs) allows control of the incident illumination from varying angles. This combines concepts from multi-view stereo imaging and gonioreflectometry to permit 3D reconstruction and surface reflectance modeling as shown in Fig. 1. Our benchtop prototype provides approximately $1\,\mu\mathrm{m}$ horizontal spatial resolution and $5\,\mu\mathrm{m}$ vertical 3D reconstruction resolution. We further present the design of a miniaturized version fitting within a volume of $300\,\mathrm{cm}^3$ and weighing less than $150\,\mathrm{g}$ made from commercial-off-the-shelf parts. With improved packaging, we are confident $150\,\mathrm{cm}^3$ and $100\,\mathrm{g}$ is possible, placing it well within the required parameter space for ruggedized miniature remote sensing payloads such as our projectile-delivery concept shown in Fig. 2. While the performance of this miniaturized version is not yet studied in detail, its fundamentally identical optical concept and our initial testing suggest that the same performance can be expected. We additionally neglect integrated computing and data transmission, however this should present little hurdle in any final application given the state of contemporary micro-electronics.

We rigorously validate the efficacy of our device for 3D reconstruction by nanofabricating a novel fiducial target whose geometry was specifically designed to test differing sources of error. With this 3D-fiducial, we demonstrate performance comparable to a lab-grade microscope which relies on precision mechanical motion to recover height information. We further demonstrate imaging of a number of planetary soil simulants characteristic of the surface of the Moon, Mars, and an asteroid to illustrate the value of 3D microscopy in field contexts. Finally, we enumerate several of many potential capabilities of such a device, including soil grain classification to identify the regional makeup of a given sample and our ambitious plans to extend this work by incorporating more advanced computational techniques for reconstruction and rendering.

Such a device could provide a revolutionary increase in contextual awareness for scientific and inspection tasks in which the subject specialist cannot be present at the location of the sample, as in planetary exploration or generally any remote hazardous area. Dynamic 3D renderings of an object from multiple viewpoints (as this enables), can provide a level of immersion similar to holding an enlarged version of the object in one's hand, even from across the solar system.

### A. Related work

Robotic remote sensing, particularly in planetary exploration, has long been a fertile proving ground for numerous sensors providing insight, often through clever indirect measurements into the structure, formation, and potential habitability of other planets. For various reasons including risk aversion and limited onboard processing, uses of computational imaging have been limited to relatively common techniques such as stereoscopic photography, mosaicing for panorama generation, stacking of differently filtered exposures for multi-spectral imaging, and dewarping of images in systems using hemispherical lenses or mirrors for wider situational awareness around the vehicle [5]. As miniaturization and power efficiency of electronics continue to progress, these applications present a ripe opportunity for broadly increased uses of computational imaging.

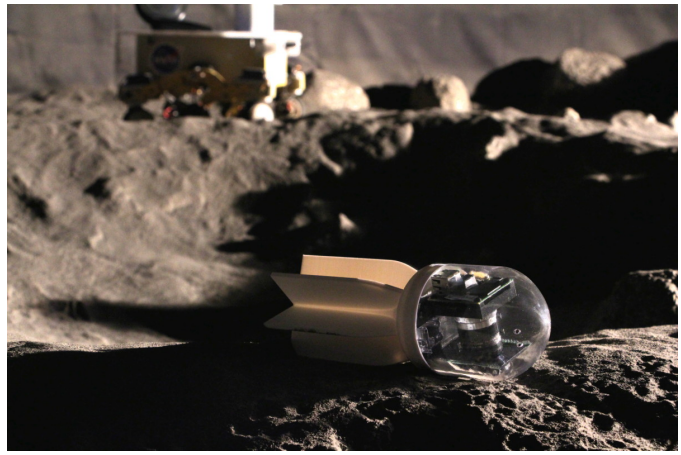

Fig. 2. Miniaturized prototype microscope installed as a rover-deployed projectile payload, demonstrating a remote sensor concept for hazardous terrain inaccessible to the parent vehicle.

Microscopy is a highly desirable capability in field exploration, an early example of which is the hand-held Apollo Lunar Surface Close-Up Camera carried by the Apollo 11 and 12 missions, which provided stereo pairs with $80\,\mu\mathrm{m}$ resolution of the Moon's surface [6]. The more recent Mars rovers are likewise no exception, each including a microscope mounted on an extending instrument arm. The Microscopic Imager (MI) instrument on the Mars Exploration Rovers (Spirit and Opportunity) provide images with magnification up to $30\,\mu\mathrm{m}$ per pixel [7], and the more advanced MAHLI instrument on Curiosity provides an increased $14\,\mu\mathrm{m}$ per pixel [1]. Our device is intended to operate in a more diminutive scale regime suited to examine the structure of individual regolith grains. Prior grain size studies of Apollo lunar mission samples found median grain sizes ranging from approximately 30 to $100\,\mu\mathrm{m}$ [8]. Recently, compact micro-rovers suitable for remote deployment from a parent vehicle such as the JPL PUFFER [9] have been proposed, along with the use of a macro lens attached to a smartphone-scale CMOS camera to form a remote microscopic imager. Similar constructions have been used for in-situ animal brain fluorescence imaging [10].

Traditionally, sample inspection microscopy is conducted using a stereo microscope having two distinct optical paths, providing images from two separated viewpoints providing the user slightly shifted images to either eye. 3D reconstruction can in principle be attained from this information using stereo

disparity correlation. Stereo imaging is a special case of light-field or multi-view imaging, a now highly popular technique for geometric reconstruction [11]. Since multi-camera setups are cumbersome, existing work has reduced this to a single optical path using a coded or programmable aperture, providing an analogous perspective shift as the aperture is varied, using for instance an LCD [12]. Another means is to insert a microlens, or lenslet, array generating an image similar to that of a compound arthropod eye. This has seen use in both microscopy [13] and recently marketed commercial plenoptic cameras such as the Lytro Light-Field Camera. This allows for limited virtual refocusing but greatly reduces the effective image resolution. With stereo microscopy now primarily relegated to live inspection by human operators, more commonly a so-called z-stack of images is captured at varying focus distances, from which structure is recovered using depth-from-defocus techniques [14]. This requires only one optical path but relies on moving either the sample or lenses with precision linear actuators. Recent advances have enabled forming this z-stack optically, but requires complex systems currently only suitable for laboratory use [15]. In this work, we adopt the use of light-field imaging with a programmable LCD aperture to produce images from different perspectives at the full camera resolution.

Our imaging is further enhanced with controlled illumination. Deriving additional information from the effects of varied illumination has found use in diverse imaging applications. A general class of approaches under the umbrella of photometric stereo [16] (known as shape-from-shading for a single image) takes advantage of the varying appearance, particularly shadowing, of objects of based on their height and orientation as illumination is changed, enabling geometric reconstruction [17]. Such methods have previously been used in space applications such as 3D mesh enhancement for planetary environments [18], where the sun acts as a powerful varying light source. This concept has also been applied to microscopy [19] where reproduction of fine microstructure has been demonstrated for opaque samples. Beyond shape reconstruction, variable sample illumination provides rich information on important optical properties such as specularity and translucency which greatly aid specialists in the classification of objects in the sample.

The fusion of direct 3D measurements with photometric stereo has been previously demonstrated, e.g. by the use of a temporal stereo triangulation scanner for the initial depth measurement [20]. In this work, we adapt these methods to the microscopy context which to our knowledge has not been previously done, and especially not in a portable system suitable for in-situ measurements. The use of thick non-transparent samples (e.g. rocks) further distinguishes our application from recent fluorescence and confocal microscopy research, requiring a reflectance rather than transmissive optical approach.

## II. Physical device

### A. Design

The microscope forms a magnified image with two lenses. The objective lens gathers the light from a sample in the focal plane and the tube lens focuses this onto a camera sensor in the image plane. A programmable aperture is placed behind the objective lens which only lets a subset of the rays from the sample reach the camera. To achieve telecentricity the aperture is positioned one focal length behind the objective lens [13]. This ensures the image of an object is captured from the same angle irrespective of its position in the field of view (FOV) and that the size remains constant if the object is moved towards or away from the objective lens. (Telecentricity is not required but will be assumed to simplify the analysis.) Objects protruding from the focal plane appear to shift position if the aperture is moved off-axis, as shown in Fig. 3. This parallax shift $p$ depends linearly on object height $h$ as

$$p = h\frac{a}{f_o} \tag{1}$$

where $a$ is the aperture distance off-axis and $f_o$ is the objective lens focal length. The aperture diameter $d$ controls the diffraction spot size $r$ [21] and DOF of the image:

$$r = \lambda\frac{f_o}{d} \qquad \mathrm{DOF} = 2\lambda\left(\frac{f_o}{d}\right)^2 \tag{2}$$

where $\lambda \approx .5\,\mu\mathrm{m}$ is the wavelength of visible light. To achieve deep focus required for many samples the aperture should be kept small (e.g. $f_o/d \approx 10$; $r = 5\,\mu\mathrm{m}$, $\mathrm{DOF} = 100\,\mu\mathrm{m}$) but

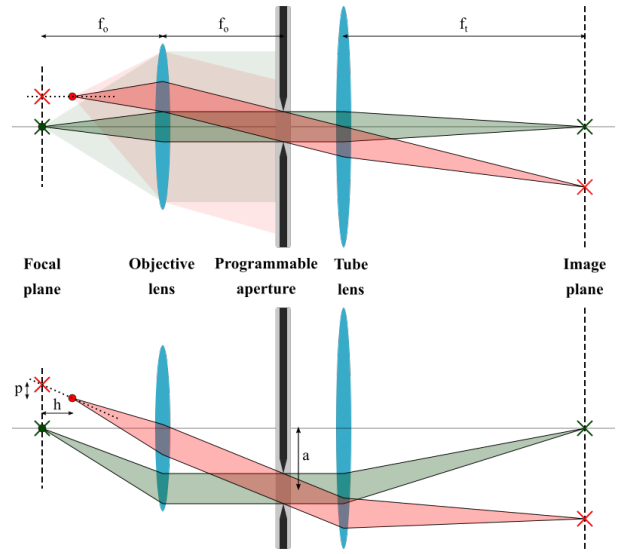


Fig. 3. Optics of microscope with programmable aperture. Two objects (disks) and their apparent position in the focal plane (crosses). Objects outside the focal plane shift due to parallax when the aperture is moved off-axis.

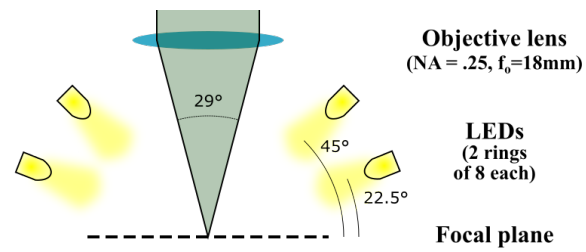


Fig. 4. Geometry of illumination and optics at the focal plane.

the programmable aperture provides flexibility for shallower images with higher resolution depending on the sample.

Reflectometry is realized with several individually controlled LEDs fixed on a hemispherical surface, shown in Fig. 4. By controlling both the active LED and the aperture position the incoming and reflected beam directions are determined, effectively forming a gonioreflectometer. The limited angular reach is significantly remedied by acting at the microscale where the shape of the sample can be exploited. By measuring the same object (e.g. a pebble) at several points with different normal directions the missing angles can be "filled in."

### B. Implementation

Fig. 1 shows the prototypes created for this work. The data presented is from the benchtop version, however, the miniature is optically similar and has been tested to work as expected. The miniature weighs $136\,\mathrm{g}$ and measures $8{\times}6{\times}6\,\mathrm{cm}^3$. The benchtop version uses a *Plan N 10x/.25* $f_o = 18\,\mathrm{mm}$ objective lens [Olympus, Japan] and a *HF75HA-1B* $f_t = 75\,\mathrm{mm}$ tube lens [Fujifilm, Japan] mounted to a *Manta G-146C* camera [Allied Vision, Germany]. The transparent LCD *DOGM128S-6* [Electronic Assembly, Germany] and *VLHW4100* narrow beam white LEDs [Vishay, USA], both controlled from a *Teensy 3.2* microcontroller [PJRC, USA], form the aperture and illumination systems. The miniature uses a $f_o = 12\,\mathrm{mm}$ *49-656* objective lens [Edmund Optics, USA], a $f_t = 50\,\mathrm{mm}$ *HF50HA-1B* tube lens [Fujifilm, Japan], a *uEye UI-5254LE* camera [IDS, Germany], and retains the other components.

For the benchtop prototype the camera pixel size of $4.65\ \mu\mathrm{m}$ and the magnification $M = 75/18 = 4.2$ gives a digital sampling of $1.12\ \mu\mathrm{m/px}$. Throughout this work, we capture images from twelve $d = 1.5\ \mathrm{mm}$ aperture disks in a non-overlapping hexagonal pattern, giving an expected spot size and DOF of $r = 6\ \mu\mathrm{m}$ and $\mathrm{DOF} = 144\ \mu\mathrm{m}$ respectively. However, the programmable aperture lends the flexibility to image with larger focal ratio and therefore resolution up to $r = 1\ \mu\mathrm{m}$ is readily available for suitable samples.

## III. 3D Reconstruction

Images captured with varying observation angles (programmable aperture) and illumination angles (controlled lighting) provide two independent methods for shape estimation. First, the parallax between all aperture positions is used to directly estimate a height-map using in a multi-view stereo (MVS) algorithm. Second, the varying intensity of the sample during different lighting conditions is used to estimate the normal vectors with a photometric stereo (PS) algorithm. Finally, these results are fused to a single shape estimate. Fig. 6 provides an example of the reconstruction process which is detailed in this section.

### A. Multi-view stereo (MVS)

An MVS correlation algorithm is implemented to reconstruct the height map of the sample. The correlation score for a candidate height is measured by translating the image pair according to (1), and calculating the normalized cross

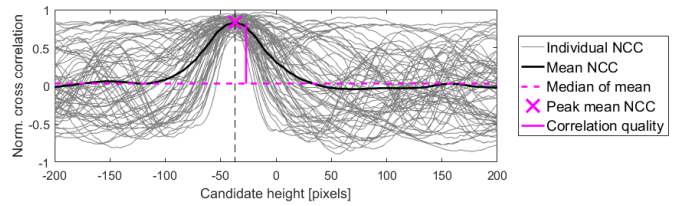


Fig. 5. Extracting a pixel's MVS height and quality. The 66 individual NCCs and the mean NCC are shown. The peak of the mean NCC determines the pixel height and correlation quality.

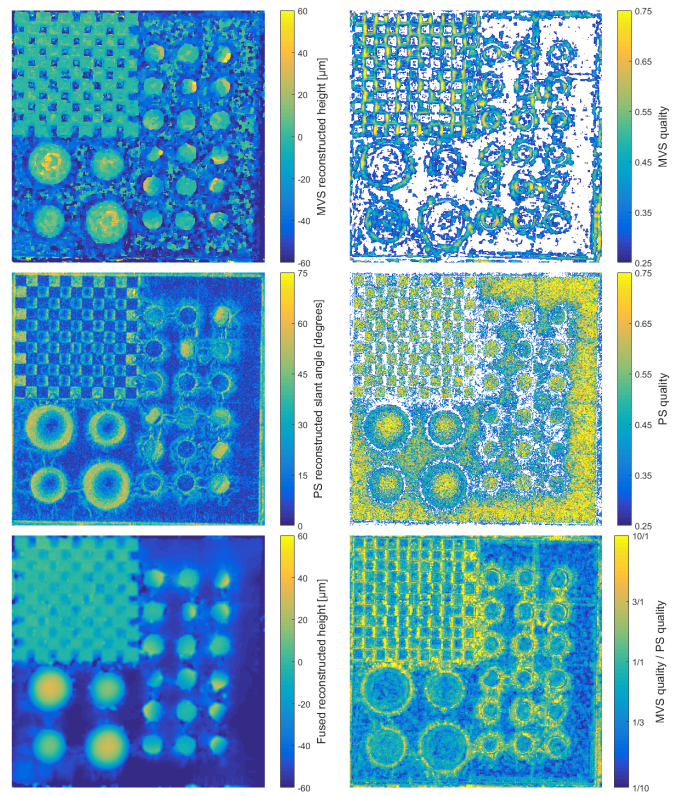


Fig. 6. 3D reconstruction steps for the 3D-fiducial presented in Section IV-B. Top: Height-map and correlation quality (< .25 blank) recovered from MVS. Middle: Normal vector slant angles and quality score (< .25 blank) from PS. Bottom: Fused MVS and PS height-map and the ratio of MVS to PS quality.

correlation (NCC) between the images for a small window centered around each pixel. The NCC between two windows with pixel values $a_i$ and $b_i$ respectively is defined as [22]:

$$\mathrm{NCC}(\mathrm{a},\mathrm{b}) = \frac{\sum_i (a_i - \bar{a})(b_i - \bar{b})}{\sqrt{\sum_i (a_i - \bar{a})^2 \sum_i (b_i - \bar{b})^2}} \tag{3}$$

where bar denotes the mean. The NCC is calculated using a $15{\times}15$ pixel window and for every unique aperture pair. The mean of the NCC across all aperture pairs is found and the candidate height with the greatest mean NCC is taken to be the height $h$ at this pixel. The quality of the correlation is taken as the difference between the greatest and median value of the mean NCC. This process, as demonstrated in Fig. 5, effectively rejects spurious correlation in individual image pairs, allowing correlation with a small window. The height map is refined by discarding all points with quality below .25 and applying Garcia's robust automated smoothing [23] with the quality as weights on the remaining points to "inpaint" the discarded z-values and remove outliers.

### B. Photometric stereo (PS)

Recovery of normal vectors is performed by classical PS [16] formulated as a matrix equation with a Lambertian reflectance model. This choice of model allows normal vector recovery on a pixel-by-pixel basis with little computational time.

Consider illuminating a sample with normal vector $\hat{\mathbf{n}}$ by a point light source from direction $\hat{\mathbf{l}}$. In the Lambertian model the intensity must satisfy:

$$i = \rho \hat{\mathbf{l}} \cdot \hat{\mathbf{n}} \tag{4}$$

for some scalar $\rho$. With measurements of the intensity $\mathbf{i} = [i_1, i_2, \cdots, i_m]$ produced for each individual light source $\mathbf{L} = \left[\hat{\mathbf{l}}_1, \hat{\mathbf{l}}_2, \cdots, \hat{\mathbf{l}}_m\right]$, the normal vector is estimated by finding the least-squares solution $\mathbf{n} = \rho\hat{\mathbf{n}}$ to:

$$\mathbf{L}^T \mathbf{n} = \mathbf{i} \tag{5}$$

This is extended to solve for the $P$ pixels in the image at once by forming a $P \times m$ matrix $\mathbf{I}$ of measured intensities and solving for $\mathbf{N}$ in a least-squares sense:

$$\mathbf{L}^T \mathbf{N} = \mathbf{I} \tag{6}$$

where the $3 \times P$ matrix $\mathbf{N}$ represents the normal vector at each pixel multiplied by some scalar ($\rho$). By normalizing this gives $\hat{\mathbf{n}}_k$ at every pixel $k$.

The quality of the normal vector for pixel $k$ is primarily characterized by the root-mean-square residual:

$$R_k = \sqrt{\frac{1}{m}(\mathbf{i}_k - \mathbf{L}^T \mathbf{n}_k)^2} \tag{7}$$

Two heuristic factors are also included in the quality scoring of $\hat{\mathbf{n}}_\mathbf{k}$. Very large slant angles $\theta_k = \cos^{-1}(\hat{n}_z)$ were found to be poorly reproduced and are therefore penalized. Additionally, to preserve discontinuities in the height-map, edges are penalized by finding large changes:

$$\delta n_k = \sqrt{\left(\frac{\partial \hat{n}_{x,k}}{\partial x}\right)^2 + \left(\frac{\partial \hat{n}_{y,k}}{\partial y}\right)^2} \tag{8}$$

where differentiation is attained by the Sobel [24] operators:

$$\frac{\partial \hat{n}_x}{\partial x} \approx \frac{1}{8}\hat{n}_x * \begin{bmatrix} -1 & 0 & 1 \\ -2 & 0 & 2 \\ -1 & 0 & 1 \end{bmatrix} \qquad \frac{\partial \hat{n}_y}{\partial x} \approx \frac{1}{8}\hat{n}_y * \begin{bmatrix} 1 & 2 & 1 \\ 0 & 0 & 0 \\ -1 & -2 & -1 \end{bmatrix} \tag{9}$$

The PS quality score is now defined as:

$$q_{PS,k} = 2^{-(R_k/.2)^2} \cdot 2^{-(\theta_k/80^\circ)^2} \cdot 2^{-(\delta n_k/.1)^2} \tag{10}$$

Normal vectors with quality below .25 are discarded.

### C. Height and normal vector fusion

Ideally, the measurements of MVS and PS agree everywhere:

$$\left.\frac{\partial Z}{\partial x}\right|_k = -\frac{\hat{n}_{x,k}}{\hat{n}_{z,k}} \qquad \left.\frac{\partial Z}{\partial y}\right|_k = -\frac{\hat{n}_{y,k}}{\hat{n}_{z,k}} \tag{11}$$

In reality however, the success of the respective measurements are highly dependent on the features present in the sample. MVS and PS measurements are complementary, as smooth monotone areas are well reproduced by PS but difficult for MVS, and vice versa. We take advantage of this fact by fusing the measurements with an adaptation of Nehab et al.'s method [20] to telecentric geometry and with weighted measurements. In the low-quality measurement regime this method can be interpreted as finding the surface which agrees with the MVS height-map at points where MVS quality is comparatively good, and spanning the remaining areas with the surface which best follows the PS normal vectors.

Let the measured MVS height-map be reshaped to a $P \times 1$ vector $\mathbf{z}^{\mathrm{MVS}}$, and form the local slopes measured by PS $\mathbf{s}_x^{\mathrm{PS}} = -\hat{n}_x/\hat{n}_z$ and $\mathbf{s_y}^{\mathrm{PS}} = -\hat{n}_y/\hat{n}_z$, also shaped to $P \times 1$ vectors. Differentiation is approximated by the sparse $P \times P$ matrices $\mathbf{T}_x$ and $\mathbf{T}_y$ which, when acting on $\mathbf{z}$, calculates the Sobel operators, see (9). Furthermore, let $\mathbf{Q}_{\mathrm{MVS}}$ and $\mathbf{Q}_{\mathrm{PS}}$ be $P \times P$ diagonal matrices with the MVS and PS qualities respectively. The cost function to be optimized is now formed as:

$$\begin{aligned} E_\lambda(\mathbf{z}) = &\lambda^2 \left\|\mathbf{Q}_{\mathrm{MVS}}\left(\mathbf{z} - \mathbf{z}^{\mathrm{MVS}}\right)\right\|^2 \\ &+ \left\|\mathbf{Q}_{\mathrm{PS}}\left(\mathbf{T}_x\mathbf{z} - \mathbf{s}_x^{\mathrm{PS}}\right)\right\|^2 \\ &+ \left\|\mathbf{Q}_{\mathrm{PS}}\left(\mathbf{T}_y\mathbf{z} - \mathbf{s}_y^{\mathrm{PS}}\right)\right\|^2 \end{aligned} \tag{12}$$

where $\lambda$ is a scalar which determines the equivalence of MVS and PS deviation. Heuristically we find that $\lambda = .05\,\mathrm{rad}/\mu\mathrm{m}$ (about $3^\circ/\mu\mathrm{m}$) gives good fusion and is used throughout. The surface minimizing this function, $\tilde{\mathbf{z}} = \arg\min_\mathbf{z} E_\lambda(\mathbf{z})$, is the ordinary least squares solution to the matrix equation:

$$\begin{bmatrix} \lambda\mathbf{Q}_{\mathrm{MVS}} \\ \mathbf{Q}_{\mathrm{PS}}\mathbf{T}_x \\ \mathbf{Q}_{\mathrm{PS}}\mathbf{T}_y \end{bmatrix} \tilde{\mathbf{z}} = \begin{bmatrix} \lambda\mathbf{Q}_{\mathrm{MVS}}\mathbf{z}^{\mathrm{MVS}} \\ \mathbf{Q}_{\mathrm{PS}}\mathbf{s}_x^{\mathrm{PS}} \\ \mathbf{Q}_{\mathrm{PS}}\mathbf{s}_y^{\mathrm{PS}} \end{bmatrix} \tag{13}$$

In which the matrix is $3P \times P$ and sparse with $13P$ nonzero elements, which is readily solved with standard sparse solvers.

## IV. Experimental evaluation

### A. Calibration

A standard microscope scale was imaged to confirm the expected pixel scale of $1.12\,\mu\mathrm{m}/\mathrm{px}$ in the plane. To calibrate the z-dimension a 2D-grid was placed on a micrometer-driven linear stage and moved in steps of $10\,\mu\mathrm{m}$, see Fig. 7. The MVS algorithm of Section III-A was applied to the data, with the correlation window set to the full image size. The measured z-scale of $1.26\,\mu\mathrm{m}/\mathrm{px}$ is slightly larger than the expected value due to our prototype not being perfectly telecentric. The RMS residual of the fit, $1.9\,\mu\mathrm{m}$, represents a lower bound on the MVS correlation accuracy.

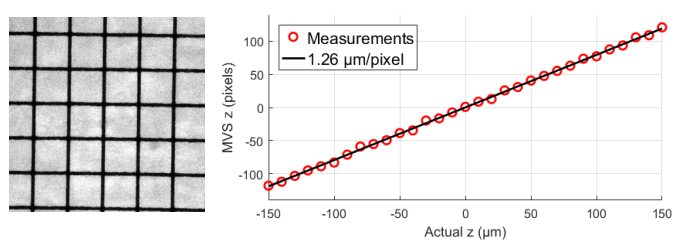


Fig. 7. The $200\,\mu\mathrm{m}$ square grid shown on the left was moved axially with a linear stage to calibrate the MVS height-maps.

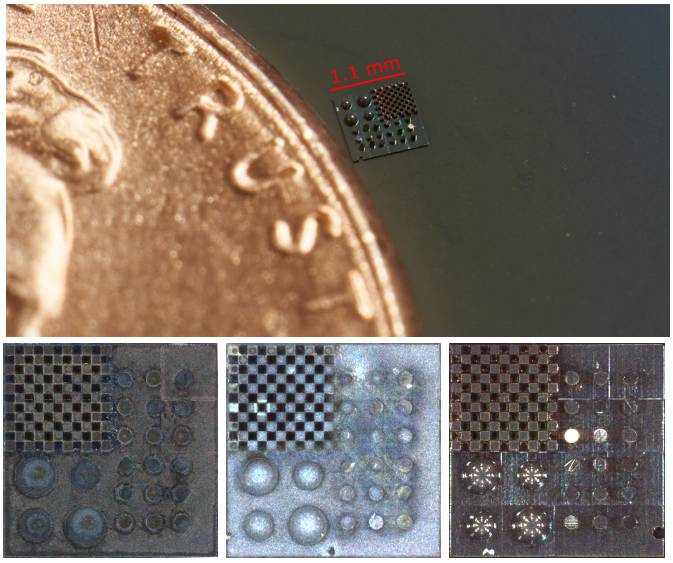


Fig. 8. Top: Macro-image of the manufactured 3D-fiducial next to a US penny for scale. Bottom row: The three versions of the device used for performance evaluation in this work. Corroded by (L to R): Oxygen (O) plasma for 75 s; sulfur bath followed by O plasma for 30 s; O plasma for 45 s.

### B. 3D-fiducial design and manufacturing

To our knowledge, there exists no suitable microscopy 3D-fiducials to quantitatively calibrate and test reconstruction performance, which has led to previous work either imaging uncalibrated devices, e.g. a small capacitor or lenslet array [25], or a 2D-fiducial mounted to a wedge [26]. Therefore, a significant effort was put into design and nanofabrication of a novel device for this purpose, shown in Fig. 8. The 3D model is available as supplementary material and is suitable for scaling up or down to match other imaging systems. The version used here is intended for measuring a $1\times1\,\mathrm{mm}^2$ field of view with $100\,\mu\mathrm{m}$ depth. The 3D-fiducial includes three sets of test features intended to test different important properties of the reconstruction:

1) A checkerboard with $50\times50\,\mu\mathrm{m}^2$ fields and $50\,\mu\mathrm{m}$ depth to measure distortion across the field of view, the uniformity of the reconstruction, and the accuracy of reproducing simple features.
2) 18 slanted planes with randomly chosen angles and directions to measure the accuracy of normal vector reproduction and complex shape reproduction.
3) Four hemispheres with radii of $75\,\mu\mathrm{m}$ and $100\,\mu\mathrm{m}$ to measure the full range of normal vector reproduction, and the reconstruction of smooth shapes.

The fiducials were manufactured in a commercial *Photonics Pro. GT* two-photon polymerization 3D printer [Nanoscribe, Germany] using $500\,\mathrm{nm}$ layer height on an ITO (Indium Tin Oxide) coated glass substrate. $5\,\mathrm{nm}$ of chromium followed by $100\,\mathrm{nm}$ of silver was sputtered onto the surface. Several of these silvered fiducials were created and subsequently corroded using different methods to provide a range of challenging devices to test our system. The three final subjects provide a full range of reflectance properties for PS, from dull to highly specular. They further provide a challenge for MVS with relatively little micro-texture compared to real materials.

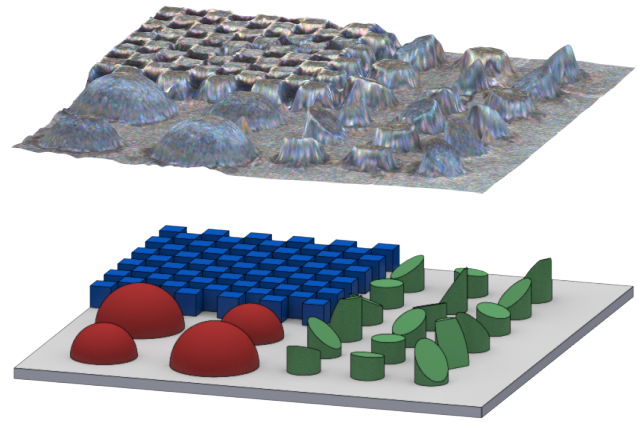

Fig. 9. Top: Reconstructed 3D-fiducial ($O_2$ long) with image texture added. Bottom: Render of the 3D-fiducial from the same viewing direction.

TABLE I
MEAN ABSOLUTE ERROR IN µm FOR RECONSTRUCTION OF THE 3D-FIDUCIALS. RESULTS ARE PRESENTED FOR THE FULL FIDUCIAL, AS WELL AS THE THREE TEST SECTIONS. AS REFERENCE THE FULL FIDUCIAL MEASURED BY A COMMERCIAL MICROSCOPE Z-STACK IS INCLUDED.

| *Fiducial version:* | *Our MVS+PS fusion error in microns:* | | | | *Zeiss z-stack:* |
|---|---|---|---|---|---|
| | *Checker* | *Planes* | *Hemisph.* | *Full* | |
| $O_2$ long | 1.9 | 4.9 | 7.1 | 11.0 | 17.2 |
| LoS+$O_2$ | 2.2 | 6.1 | 5.6 | 14.4 | 6.0 |
| $O_2$ short | 2.1 | 6.4 | 9.1 | 13.1 | 10.0 |
| **Average** | **2.1** | **5.8** | **7.3** | **12.8** | **11.1** |

### C. Commercial reference microscope

The finished fiducials were measured in a conventional commercial microscope to verify their properties and provide a comparison to our methods. This was done with an *Axio Imager M2m* microscope with an *EC Epiplan 5x/.13* objective and an *Axiocam ICc5* camera [all from Zeiss, Germany]. This resulted in images with $.69\,\mu\mathrm{m/px}$ resolution and an approximate DOF of $15\,\mu\mathrm{m}$, from (2). A focus stack consisting of 31 images separated by $5\,\mu\mathrm{m}$ was recorded and the *Fiji* [27] plugin *Stack Focuser* was used with a $5\times5$ pixel window to create a height-map. Finally it was smoothed with a Gaussian blur (standard deviation of 3 pixels).

## V. RESULTS

### A. 3D performance

By application of the fused MVS and PS method presented in Section III to data captured from the 3D-fiducials the resulting shape can be quantitatively evaluated compared to the ground-truth shape of the fiducial, shown in Fig. 9. The mean absolute error (MAE) is used as performance metric, presented in Table I. Measurements of the test features show a precision of around $2\,\mu\mathrm{m}$ and $7\,\mu\mathrm{m}$ for simple and challenging shapes respectively. Additionally, measurements of the full fiducial shape (all features and the base) shows a global accuracy of $13\,\mu\mathrm{m}$, similar to the performance attained from the commercial reference microscope z-stack. Although not directly measured, these results and the z-calibration residual ($1.9\,\mu\mathrm{m}$ RMS) suggest a height resolution of around $5\,\mu\mathrm{m}$.

Qualitatively we also observe that the reconstructed surfaces closely resemble the underlying shape, with excellent preservation of smooth shapes (hemispheres), good handling of discontinuities, and a consistent result across the checkerboard pattern. Steeply slanted planes and the dark areas between the checkerboards are found most difficult to reconstruct, however the degradation of these areas is handled well, by resulting in less steep slanted planes and cup-shaped holes between the checkerboards respectively.

### B. Planetary simulant results

We have imaged a large catalog of planetary regolith simulants to test the system in field-like situations. In Figs. 10–12 we present data from three samples of research simulants for an asteroid, Mars, and the Moon respectively. In these real-world scenarios we observe an MVS correlation quality which is on average $2\times$ that of the fiducials, while the PS quality is around 20% better — implying that we can attain at least the measured performance on real samples.

These results show the striking microscopic difference between samples which with lower resolution look similar. Several similarities and differences can be picked out even by an untrained observer. Especially striking is the white and highly specular prolate grain to the left in the asteroid simulant. This sits at an angle and measures roughly $300\,\mu\mathrm{m}$ in length and $100\,\mu\mathrm{m}$ in waist width. The asteroid and lunar simulants share an overall appearance of rough, irregular grains with several highly specular small protrusions. Contrasting to this, the major component of the martian simulant is rounded, dull, red-brown grains ranging widely in size. Scattered around the sample are various other grains which are dark, rough, and have a metallic sheen. By closely examining this kind of features and comparing samples retained from different regions, a specialist is able to draw detailed conclusions about the formation and history of major planetary features. To further aid in this, we demonstrate rendering novel views from new perspectives (shown here) or lighting conditions (shown in Fig. 1) which, especially when viewed interactively, provide immersion and nuance not otherwise possible.

## VI. Extensions and Future Work

We envision several avenues of promising future work. Of special interest to us are in-situ bidirectional reflectance distribution function (BRDF) recovery and optical material classification. With a known height-map and normal vector field already demonstrated, the local lighting and observation geometry (including occlusions) can be recovered and a physical reflectometric model fitted to the measurements. Full modeling allows capturing the finest visual details and inferring physical sample properties without mechanical actuation, to enable automated sample analysis. These methods can be greatly enhanced by modifying the system to use specific wavelengths to exploit spectroscopic features (e.g. fluorescence) or by measuring the strong polarization effects of reflected light.

A major hardware goal is to create a device with passive focusing. A promising concept for this is to place a window

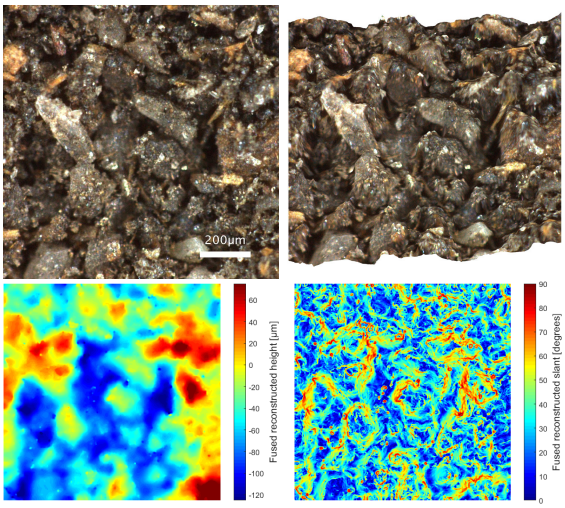


Fig. 10. Asteroid simulant *DS-1-CR-1* measured in our system. A: Microscope image with centre aperture and full illumination. B: Rendered oblique view (30° tilt) from the reconstructed 3D data. C and D: Reconstructed fused height-map and normal vector slant angles respectively.

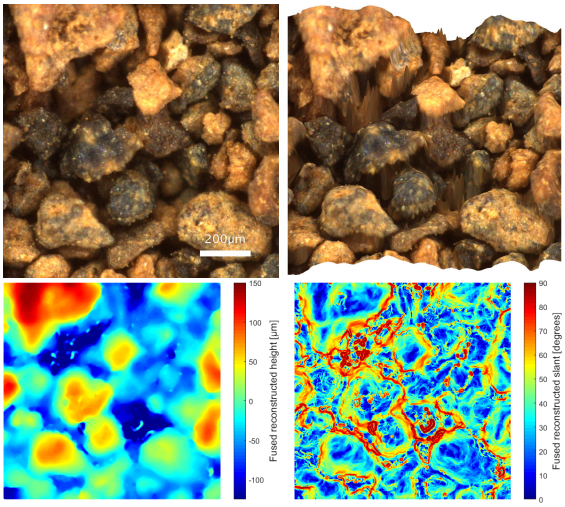


Fig. 11. Martian regolith simulant *JSC Mars-1*, same views as in Fig. 10.

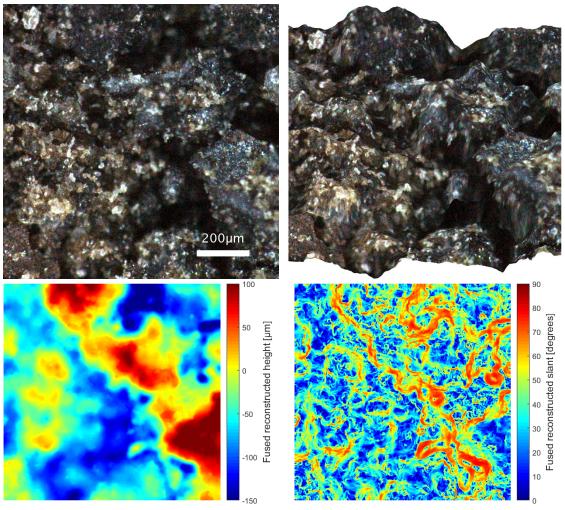


Fig. 12. Lunar regolith simulant *JSC-1A*, same views as in Fig. 10.

just inside the focal plane for the system to gently rest on. We have proven the feasibility of this by capturing practically unaltered data through a sapphire window placed in direct contact with the sample. Preliminary designs for a handheld prototype combining this concept with an optics and electronics upgrade providing a greater field of view have been created. With this device we seek to further prove the efficacy of our concept as a tool for exploration.

From a practical standpoint there remain open questions concerning the device's tolerance to space environments, especially radiation and temperature. Understanding if there are major fault modes and how these can be alleviated or circumvented remains an interesting topic which could continue the present trend in expanding electronics capabilities in space applications.

The 3D-fiducial presented here is intended as a general use target, giving an overview of the system performance in a broad range of scenarios. However, we have identified several possible developments with this manufacturing method. First, more specialized targets, such as dense lines for direct resolution measurements in all dimensions are possible. Second, adding random depth micro-texture at the layer thickness ($\pm 500\,\mathrm{nm}$) should enable surface roughness more similar to natural materials. Third, by coating the 3D-fiducial in materials with known reflection characteristics (e.g. BRDF), reflectometric calibration and accuracy may also be measured.

## VII. Conclusion

Future space and terrestrial field exploration increasingly target hazardous, poorly-accessible areas requiring compact ruggedized sensor payloads. Towards a means of surface micro-inspection, we present a novel light-field microscope for 3D reconstruction suitable for highly payload-constrained systems. Validation against a custom calibration fiducial demonstrates performance comparable to existing benchtop 3D lab microscopes, but in a miniature solid-state format. Not only can this provide distant scientists with an immersive perspective of the geometry and optical properties of surfaces, but through further interpretation of the reflectometry can offer insight into the composition and substructure of constituent materials. We believe this represents just one of many possible means of overcoming physical limitations of remotely fielded sensors via a computational imaging approach.

## Acknowledgment

The authors thank Terry Fong at NASA and Gunnar Tibert at KTH for endorsing this collaboration. We also thank Antoine Tardy, Benjamin Lehner, Eric Johnston, Meredith Metzler, and Demis John for their help in parts of this project. G. M. Pettersson's work at the NASA Ames Research Center was supported by the Swedish National Space Administration. This project was supported by the NASA Ames Internal Research and Development Fund. We thank NASA SSERVI for use of regolith simulant samples. This work was carried out in part at the Univ. of Pennsylvania Singh Center for Nanotechnology which is supported by the NSF under grant NNCI-1542153.

## References

[1] K. S. Edgett *et al.*, "Curiosity's Mars hand lens imager (MAHLI) investigation," *Space Science Reviews*, vol. 170, no. 1, pp. 259–317, Sep 2012.

[2] G. Landis, S. Oleson, and M. McGuire, "Design study for a Mars geyser hopper," in *AIAA Aerospace Sciences Conference*, no. AIAA-2012-0631, 2012.

[3] P. Abad-Manterola *et al.*, "Axel: A minimalist tethered rover for exploration of extreme planetary terrains," *IEEE Robotics and Automation Magazine*, vol. 16, no. 4, pp. 44–52, 2009.

[4] B. Balaram, T. Canham, C. Duncan, H. Grip, W. Johnson, J. Maki, A. Quon, R. Stern, and D. Zhu, "Mars helicopter technology demonstrator," in *AIAA Atmospheric Flight Mechanics Conference*, 2018.

[5] L. Matthies *et al.*, "Computer vision on Mars," *International Journal of Computer Vision*, vol. 75, no. 1, pp. 67–92, Oct 2007.

[6] T. Gold, "Apollo 11 and 12 close-up photography," *Icarus*, vol. 12, no. 3, pp. 360–375, 1970.

[7] K. E. Herkenhoff *et al.*, "Athena microscopic imager investigation," *Journal of Geophysical Research: Planets*, vol. 108, no. E12, 2003.

[8] D. S. McKay, R. M. Fruland, and G. H. Heiken, "Grain size and the evolution of lunar soils," in *Lunar and Planetary Science Conference Proceedings*, vol. 5, 1974, pp. 887–906.

[9] J. T. Karras *et al.*, "Pop-up Mars rover with textile-enhanced rigid-flex PCB body," in *IEEE International Conference on Robotics and Automation (ICRA)*, 2017, pp. 5459–5466.

[10] K. K. Ghosh *et al.*, "Miniaturized integration of a fluorescence microscope," *Nature Methods*, vol. 8, pp. 871–878, Sep 2011.

[11] R. Hartley and A. Zisserman, *Multiple View Geometry in Computer Vision*. New York, NY, USA: Cambridge University Press, 2003.

[12] C. Zuo, J. Sun, S. Feng, M. Zhang, and Q. Chen, "Programmable aperture microscopy: A computational method for multi-modal phase contrast and light field imaging," *Optics and Lasers in Engineering*, vol. 80, pp. 24 – 31, 2016.

[13] M. Levoy, R. Ng, A. Adams, M. Footer, and M. Horowitz, "Light field microscopy," in *ACM Transactions on Graphics (TOG)*, vol. 25, no. 3, 2006, pp. 924–934.

[14] S. Chaudhuri and A. N. Rajagopalan, *Depth from defocus: a real aperture imaging approach*. Springer Science & Business Media, 1999.

[15] S. Abrahamsson *et al.*, "Fast multicolor 3D imaging using aberration-corrected multifocus microscopy," *Nature methods*, vol. 10, no. 1, p. 60, 2012.

[16] R. J. Woodham, "Photometric method for determining surface orientation from multiple images," *Optical Engineering*, vol. 19, no. 1, pp. 139–144, 1980.

[17] S. Barsky and M. Petrou, "The 4-source photometric stereo technique for three-dimensional surfaces in the presence of highlights and shadows," *IEEE Transactions on Pattern Analysis and Machine Intelligence*, vol. 25, no. 10, pp. 1239–1252, 2003.

[18] U. Wong, "Lumenhancement: Exploiting appearance for planetary modeling," Ph.D. dissertation, Carnegie Mellon University, Pittsburgh, PA, April 2012.

[19] Z. Li and Y. F. Li, "Dense and refined microstructure 3D measurement method based on an optical microscope and varying illuminations," *Measurement Science and Technology*, vol. 22, no. 3, 2011.

[20] D. Nehab, S. Rusinkiewicz, J. Davis, and R. Ramamoorthi, "Efficiently combining positions and normals for precise 3D geometry," *ACM Transactions on Graphics*, vol. 24, no. 3, pp. 536–543, Jul. 2005.

[21] E. Abbe, "Beiträge zur theorie des mikroskops und der mikroskopischen wahrnehmung," *Archiv für mikroskopische Anatomie*, vol. 9, no. 1, pp. 413–418, 1873.

[22] J. P. Lewis, "Fast template matching," in *Vision Interface*, 1995.

[23] D. Garcia, "Robust smoothing of gridded data in one and higher dimensions with missing values," *Computational Statistics and Data Analysis*, vol. 54, no. 4, pp. 1167–1178, 2010.

[24] R. O. Duda, *Pattern classification and scene analysis*. New York: Wiley, 1973, pp. 271–272.

[25] X. Lin, J. Wu, G. Zheng, and Q. Dai, "Camera array based light field microscopy," *Biomedical Optics Express*, vol. 6, no. 9, pp. 3179–3189, Sep 2015.

[26] K. E. Jensen, D. A. Weitz, and F. Spaepen, "Note: A three-dimensional calibration device for the confocal microscope," *Review of Scientific Instruments*, vol. 84, no. 1, p. 016108, 2013.

[27] J. Schindelin *et al.*, "Fiji: an open-source platform for biological-image analysis," *Nature methods*, vol. 9, no. 7, p. 676, 2012.